Aalto University
School of Science
Mater's Programme in Engineering Physics

Kukka-Emilia Huhtinen

Dynamical mean-field study of the Fulde-Ferrell-Larkin-Ovchinnikov phase in the kagome lattice

Master's Thesis
Espoo, July 19, 2018

Supervisor: Professor Päivi Törmä
Advisor: Professor Päivi Törmä

Aalto University
School of Science
Mater's Programme in Engineering Physics

ABSTRACT OF
MASTER'S THESIS

Author:	Kukka-Emilia Huhtinen		
Title: Dynamical mean-field study of the Fulde-Ferrell-Larkin-Ovchinnikov phase in the kagome lattice			
Date:	July 19, 2018	**Pages:**	46
Major:	Engineering Physics	**Code:**	SCI3056
Supervisor:	Professor Päivi Törmä		
Advisor:	Professor Päivi Törmä		

Fulde–Ferrell–Larkin–Ovchinnikov (FFLO) phases are superconducting phases in which Cooper pairs have a nonzero total momentum. Despite experimental efforts to directly observe this state, it has remained elusive, and its existence is supported only by indirect evidence.

In systems featuring a constant dispersion band, also called flat band, unconventional pairing mechanisms could help stabilize exotic superfluid phases. Those systems could thus be good candidates for a direct observation of FFLO phases.

In this work, we study FFLO state in one such system, the kagome lattice, with dynamical mean-field theory (DMFT). We use two different approaches. One is based on including the FF ansatz, an order parameter modulated by a plane wave, in cluster DMFT. The other is a partially real-space DMFT calculation. With both methods, we find a stable FFLO state in the vicinity of the flat band singularity.

Keywords:	superconductivity, FFLO, flat band, dynamical mean-field theory
Language:	English

Acknowledgments

The research included in this thesis was carried out in the Quantum Dynamics (QD) group of the Department of Applied Physics at Aalto University. I used dynamical mean-field theory codes that have been written in the QD group. Computing resources were provided by CSC.

I would like to thank my instructor Päivi Törmä for giving me the opportunity to work on this project, which taught me a lot. I am also grateful to Tuomas Vanhala, who gave valuable instructions and advice. In addition, I would like to thank other members of the QD group for insightful conversations.

Finally, I would like to thank my family and friends for their support.

Espoo, July 19, 2018

Kukka-Emilia Huhtinen

Contents

Chapter 1

Introduction

Superconductors are materials which, when cooled below a characteristic critical temperature, acquire an infinite electrical conductivity and expulse magnetic fields. The latter phenomenon is referred to as the Meissner effect, and is a key difference between classical perfect conductors and superconductors: a perfect conductor only requires a magnetic field constant in time, not that the magnetic field vanishes.

The first microscopic theory of superconductivity was devised in 1957 by Bardeen, Cooper and Schrieffer (BCS) [1]. It explains superconductivity by the formation of a condensate of Cooper pairs, pairs of fermions with different spins and opposite momenta. Such pairs form for arbitrarily small attractive interactions between fermions, provided the system has a Fermi sea [2]. BCS theory is successful at predicting various phenomena, such as the existence of an energy gap for single-particle excitations and the Meissner effect, and has provided great insight into the physics of conventional superconductors.

However, many questions remain open concerning superconductivity. One is whether it can exist in spin-density or mass imbalanced systems. Experimentally, only phase separation has been directly observed [3–6]. However, several possible spin-imbalanced superfluid phases have been proposed. One is the Fulde-Ferrell-Larkin-Ovchinnikov (FFLO) phase, first proposed independently by Fulde and Ferrell [7] and Larkin and Ovchinnikov [8] in 1962. In this phase, Cooper pairs carry finite momentum even in the ground state.

Despite great efforts to observe the FFLO state, only indirect evidence of its existence has been obtained [9–11]. One possible reason for the lack of direct observations is that the stability region for the FFLO state is small and easily missed. There are predictions that certain systems can particularly favour exotic pairing, and they can thus be good candidates for the direct observation of an FFLO phase. For example, van Hove singularities and Fermi surface nesting in lattices can enhance the FFLO phase [12, 13]. We confirm in this thesis that flat bands can also have a profound effect on the pairing mechnism as particles on a flat band can rearrange at zero energy cost, making exotic spin-imbalance pairing more favourable [14].

Another obstacle in the observation of the FFLO phase may be fluctuations that can make the state unstable [15, 16]. Some beyond mean-field studies of the FFLO phase based on dynamical mean-field theory (DMFT) [17–19] and quantum Monte Carlo (QMC) [20–22] have been done indicating it can be stable even when fluctuations are present. However, most studies are done at the mean-field level.

In this work, we study superfluidity in the kagome lattice using dynamical mean-field theory, with particular interest in the FFLO state. The main objective is to verify whether such a state is still stable when local fluctuations are taken into account. Another aim is to verify wether the flat band favours FFLO as, in mean-field theory, unconventional pairing was predicted to facilitate exotic superfluidity.

This thesis is organised as follows. In Chapter 2, we give a review of the physical background, including the Hubbard model, a presentation of the kagome lattice, and an explanation of the pairing mechanism behind FFLO phases. In Chapter 3, real-space and cluster dynamical mean-field theories are explained, as well as the methods used to study the FFLO phase. In Chapter 4, the two impurity solvers used in this work are briefly presented, and in Chapter 5, results are discussed.

Chapter 2

Physical background

Hubbard model

The Hubbard model is a simplified theoretical model for studying interacting Fermions in a lattice, originally proposed by J. Hubbard in 1963 [23]. It can be used for example to describe electrons in solids, where the atoms form a lattice of minima in the potential energy due to Coulomb interactions of the electrons with the nuclei. The Hamiltonian corresponding to the model takes the general form

$$H = H_{\text{kin}} + H_{\text{int}}, \tag{2.1}$$

$$H_{\text{kin}} = -\sum_{i,j} \sum_{\sigma} t_{i,j} c^{\dagger}_{\sigma,i} c_{\sigma,j}, \tag{2.2}$$

$$H_{\text{int}} = \sum_{i} U_i n_{\uparrow,i} n_{\downarrow,i}, \tag{2.3}$$

where $t_{i,j} = t_{j,i}$ is the hopping amplitude between lattice sites i and j, and U_i is the interaction strength at site i. The operator $c_{\sigma,j}$ annihilates a particle with spin σ at site j, and $n_{\sigma,i} = c^{\dagger}_{\sigma,i} c_{\sigma,i}$ is the particle number operator. The model therefore consists of two terms: a kinetic term allowing for the tunneling of particles between lattice sites, and an on-site interaction.

This model highly simplifies the physics of actual electrons in solids. Firstly, it assumes that there is only one non-degenerate orbital per lattice site, while atoms typically have several orbitals. This approximation can however be justified in some systems. When atoms form a solid, the electrons on the outermost shells become itinerant, while electrons on inner shells remain near the nucleus. Between these two cases, there can be orbitals in which the electrons are localized, but can tunnel to corresponding orbitals in nearby atoms. If these orbitals are non-degenerate and neither the itinerant atoms nor those on lower orbitals play an important role, the Hubbard model can be appropriate to describe the solid. The second important approximation is that interactions only occur on site: the repulsive Coulomb interaction between electrons is long-ranged, so this seems inappropriate. The itinerant electrons can however screen this interaction, making it effectively short-ranged [23, 24].

The attractive Hubbard model can, surprisingly, also represent electrons in a solid. Electrons can experience a phonon-mediated attraction [25], which can overcome the Coulomb repulsion. The idea is that electrons cause deformations in the material, which in turn affect the electrons. This is the interpretation for the BCS theory of superconductivity, which assumes an attractive interaction.

Due to advances in the field of ultracold gases, it has also become possible to realize the Hubbard model, for example with atomic gases in optical lattices [26]. In these system, the average distance between atoms is typically large compared to the range of interactions, justifying the on-site interaction approximation. Feshbach resonances [27] make it possible to tune the interaction, allowing to investigate a wide parameter region of the Hubbard model experimentally.

Despite its apparent simplicity, the Hubbard model can be solved exactly only for small systems, since the Hilbert space has dimension 4^N, where N is the number of lattice sites. One common approximation is the mean-field approximation, where fluctuations are assumed small. The operator product in the interaction term can then be rewritten

$$c^\dagger_{\uparrow,i} c^\dagger_{\downarrow,i} c_{\uparrow,i} c_{\downarrow,i} \approx \left\langle c^\dagger_{\uparrow,i} c^\dagger_{\downarrow,i} \right\rangle c_{\downarrow,i} c_{\uparrow,i} + c^\dagger_{\uparrow,i} c^\dagger_{\downarrow,i} \left\langle c_{\downarrow,i} c_{\uparrow,i} \right\rangle - \left\langle c^\dagger_{\uparrow,i} c^\dagger_{\downarrow,i} \right\rangle \left\langle c_{\downarrow,i} c_{\uparrow,i} \right\rangle . \tag{2.4}$$

This gives the BCS theory on a lattice, where the order parameter is defined as $\Delta_i = \langle c_{\downarrow,i} c_{\uparrow,i} \rangle$. While the mean-field results can give a qualitative picture of phenomena, they tend to overestimate the stability of superconducting states, as quantum fluctuations that can break pairs are neglected. To take those into account, one should use beyond mean-field methods. In this work, we use dynamical mean-field theory (DMFT), which treats local fluctuations exactly. The method is presented in more detail in Chapter 3.

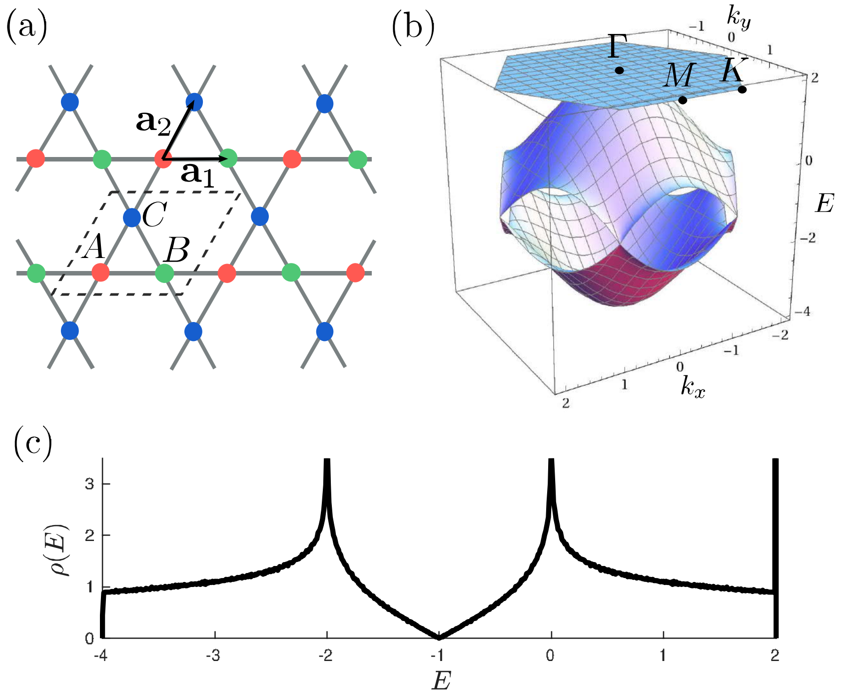

Figure 2.1: (a) Kagome lattice. The different colors indicate the three sublattices, A, B and C. The dashed lines show the unit cell, containing three sites. (b) Single-particle band structure. High-symmetry points of the Brillouin zone are indicated. The Γ point is located at the center of the Brillouin zone, K at a corner, and M at the middle of an edge. (c) The density of states, which diverges at Van Hove singularities $E = -2t$ and $E = 0$, as well as at $E = 2t$, where the flat band is located. The density of states is zero at $E = -t$ due to Dirac points.

Kagome lattice

We study an attractive Hubbard model on the kagome lattice, shown in Fig. 2.1. This is a tripartite lattice consisting in three triangular Bravais sublattices, labeled A, B and C. We assume only nearest-neighbor hopping, and equal interaction strength at all sites. The corresponding Hamiltonian is

$$H = -t \sum_{\sigma,\langle i,j\rangle} c^{\dagger}_{\sigma,i} c_{\sigma,j} - \sum_i (\mu_\uparrow n_{\uparrow,i} + \mu_\downarrow n_{\downarrow,i}) + U \sum_i \left(n_{\uparrow,i} - \frac{1}{2}\right)\left(n_{\downarrow,i} - \frac{1}{2}\right), \tag{2.5}$$

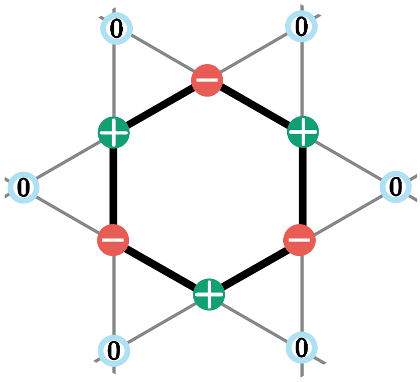

Figure 2.2: Schematic picture of a localized eigenstate on a hexagonal plaquette of the kagome lattice. The sign of the amplitude alternates between adjacent sites on the plaquette. The state is localized on the hexagon (black line) due to destructive interference.

where the sum in the first term runs over nearest neighbors. We have introduced chemical potentials μ_σ, which can be different for the two components. The subtraction of $1/2$ from the densities in the interaction term corresponds to a shift in the chemical potentials, and the addition of a constant energy $U/4$ per lattice site. In bipartite systems, this subtraction makes the interaction term explicitely particle-hole symmetric.

The single-particle band structure can be solved from the tight binding Hamiltonian

$$H_{\mathrm{kin}} = -t \sum_{\sigma,\langle i,j \rangle} c^\dagger_{\sigma,i} c_{\sigma,j}. \tag{2.6}$$

The Hamiltonian is expressed in quasimomentum space by performing a Fourier transform $c_{\sigma,i} = (1/\sqrt{N}) \sum_{\mathbf{k}} c_{\sigma,\boldsymbol{k},\alpha} e^{i\boldsymbol{k}\cdot\mathbf{R}_\mathrm{i}}$, where N is the total number of sites and the sum runs over the Brillouin zone. The index $\alpha = A, B, C$ corresponds to the sublattice of site i. The kinetic Hamiltonian in momentum space becomes

$$H_{\mathrm{kin}} = \sum_\sigma \sum_{\boldsymbol{k}} \mathbf{c}^\dagger_{\sigma,\boldsymbol{k}} H_{\boldsymbol{k}} \mathbf{c}_{\sigma,\boldsymbol{k}}, \tag{2.7}$$

$$H_{\boldsymbol{k}} = -2t \begin{pmatrix} 0 & \cos k_1 & \cos k_2 \\ \cos k_1 & 0 & \cos k_3 \\ \cos k_2 & \cos k_3 & 0 \end{pmatrix}, \tag{2.8}$$

$$\mathbf{c}_{\sigma,\boldsymbol{k}} = (c_{\sigma,\boldsymbol{k},A}, c_{\sigma,\boldsymbol{k},B}, c_{\sigma,\boldsymbol{k},C})^{\mathrm{T}}. \tag{2.9}$$

The momentum components are defined as $k_i = \boldsymbol{k} \cdot \mathbf{a}_i$, where $\mathbf{a}_1$ and $\mathbf{a}_2$ are shortest vectors between sublattices A and B, and A and C, respectively, and $\mathbf{a}_3 = \mathbf{a}_1 - \mathbf{a}_2$ (see Fig. 2.1). We take the distance between nearest neighbors as our unit length. Diagonalizing $H_{\boldsymbol{k}}$ as $H_{\boldsymbol{k}} = G_{\boldsymbol{k}} \varepsilon_{\boldsymbol{k}} G_{\boldsymbol{k}}^{\mathrm{T}}$ yields the band dispersion relations, plotted in Fig. 2.1,

$$\varepsilon_0 = 2t, \tag{2.10}$$

$$\varepsilon_{\pm} = -t \pm \sqrt{3 + 2\Lambda(\boldsymbol{k})}, \tag{2.11}$$

where $\Lambda(\boldsymbol{k}) = \sum_{i=1}^{3} \cos(2k_i)$. Notably, one of the dispersion relations is constant in momentum, giving a flat dispersion band. This arises due to localized eigenstates in the kagome lattice. These are constructed on hexagonal plaquettes by assigning amplitudes $\pm 1/\sqrt{6}$ with alternating signs to the corners (see Fig. 2.2). The tunneling to the corners of the triangles adjacent to the hexagon is then canceled by destructive interference. Localized eigenstates that are more extended in space can also be created as a superposition of eigenstates localized on different hexagonal plaquettes.

The flat band leads to a divergence of the density of states (DOS) $\rho(E)$, shown in Fig. 2.1, at energy $E = 2t$. The band structure also has other important features impacting the DOS. The Dirac cones at $E = -t$ lead to a vanishing DOS at that energy. In contrast, the saddle points on the dispersive bands at the M points of the Brillouin zone cause divergences of the DOS at energies $E = -2t$ and $E = 0$. These are called Van Hove singularities. These density features are of particular interest when studying superfluidity, as BCS theory predicts $T_c \propto \exp(-1/(U\rho(E_F)))$, where U is the interaction strength and $\rho(E_F)$ is the density of states at the Fermi energy.

Fulde-Ferrell-Larkin-Ovchinnikov phases

The BCS state cannot sustain finite polarizations. Once the chemical potential difference $|\mu_\uparrow - \mu_\downarrow|$ exceeds the Clogston limit $\sqrt{2}\Delta_0$ [28], where Δ_0 is the order parameter in the balanced case $\mu_\uparrow = \mu_\downarrow$, the phase is destroyed. However, imbalanced superfluidity can still be possible through different pairing mechanisms. Several mechanisms have been proposed, including a Sarma phase in which particles at the Fermi surface of the minority component pair with particles in the Fermi sea of the majority component [29, 30]. This phase was initially found as an unstable solution to the gap equation [29], and is indeed unstable in continuum when chemical potentials are fixed [31]. However, if particle densities are fixed instead of chemical potentials, the

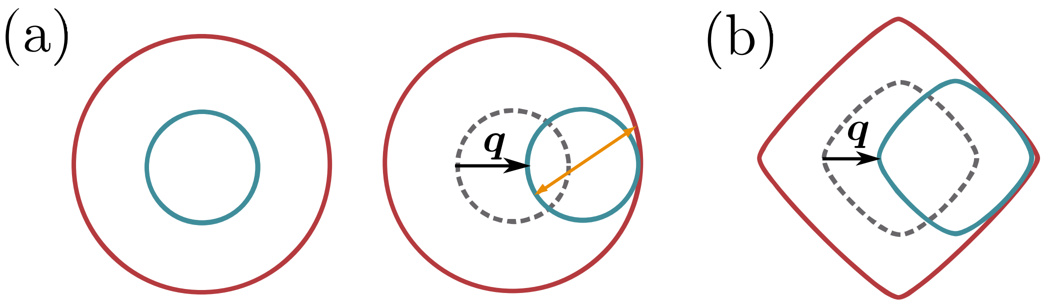

Figure 2.3: (a) Schematic representation of the conventional mechanism behind the FF state. Red and blue lines represent the majority and minority component Fermi surfaces, respectively. When the imbalance is large, the Fermi surfaces are too different for pairing to take place (left). The momentum $\boldsymbol{q}$ shifts the Fermi surface of one component, effectively matching the two. This creates a region of favourable pairing. Cooper pairs now form between particles with momenta $\boldsymbol{k}$ and $\boldsymbol{q}-\boldsymbol{k}$, and thus have a non-zero momentum $\boldsymbol{q}$. (b) In a lattice, the Fermi surfaces can have a shape such that $\boldsymbol{q}$ allows to match a large region. This is referred to as nesting. For example, in the square lattice, the Fermi surfaces are square-shapes at the Van Hove singularities.

Sarma phase can exist in continuum [32] as well as lattices [12, 33]. This type of pairing was also found to occur in multiband systems, such as a general two-band model [34], a mixed-geometry lattice [35] and the Lieb lattice [14, 36]. Another possible mechanism is Fermi surface deformation, where the Fermi surfaces of the two components are deformed to match in some regions where the pairing occurs. The deformation in this case comes at a kinetic energy cost, but remains favorable if the pairing allows to lower the energy enough [37, 38]. A third possibility, which we focus on here, is Fulde-Ferrell-Larkin-Ovchinnikov states.

This type of phases, first proposed in 1962 by Fulde and Ferrell [7], and Larkin and Ovchinnikov [8], is characterized by the formation of Cooper pairs with finite (quasi)momentum. This is translated in a spatial modulation of the order parameter, $\Delta = \Delta_0 e^{i\boldsymbol{q}\cdot\mathbf{x}}$ in the Fulde-Ferrell (FF) ansatz and $\Delta = \Delta_0 \cos(\boldsymbol{q}\cdot\mathbf{x})$ in the Larkin-Ovchinnikov (LO) ansatz, where $\boldsymbol{q}$ is the momentum of the Cooper pairs. A key difference between these two states is the symmetries they break: the LO state breaks translational symmetry, whereas the FF state breaks the time-reversal symmetry. As a consequence, density modulations are found in the LO state, but not in the FF state.

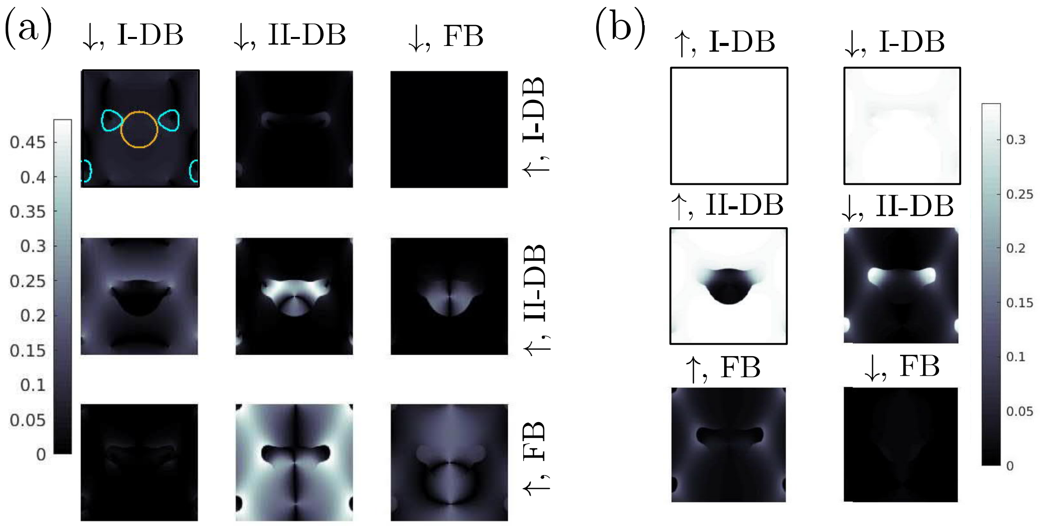

Figure 2.4: (a) Pairing correlations between different bands and (b) momentum distributions on the bands. The abreviations I-DB, II-DB and FB designate the first dispersive band, second dispersive band and flat band respectively. The orange and blue lines show the Fermi surfaces of the majority and minority components, respectively.

These two ansatzes are not the only ones possible, and a more complicated FFLO type state with more than two wavevectors $\boldsymbol{q}$ can occur.

A schematic picture explaining the typical mechanism of formation of the FF state is shown in Fig. 2.3. In the typical BCS state, pairing occurs between particles of opposite momenta near the Fermi surfaces. When the chemical potential difference is increased, the Fermi surfaces become so different that this is not possible anymore. In the FF state, one Fermi surface is shifted towards the other by a wave vector $\boldsymbol{q}$, creating a region of favorable pairing between particles of momenta $\boldsymbol{k}$ and $-\boldsymbol{k} + \boldsymbol{q}$. Even though the Cooper pairs have net momentum $\boldsymbol{q}$, there is no net current: the momentum of the unpaired particles balances that of the Cooper pairs [13].

In addition to the size, the shapes of Fermi surfaces have an important effect on the stability of the FF phase, as they influence the size of the region that can be matched. As a consequence, FFLO states can be more favorable in lattices, where the Fermi surfaces can have a high degree of nesting. For example, in the square lattice, the Fermi surfaces are square-shaped at the Van Hove singularities, which allows to match larger regions than in the case of spherical Fermi surfaces [12, 39, 40]. In the kagome lattice, the Fermi surface is hexagonal at the Van Hove singularities, a shape which is also advantageous for nesting.

In lattices with a flat band, the pairing mechanism in the FF state is different [14]. In addition to the conventional shift of a Fermi surface, a deformation of the momentum distribution of particles on the flat band occurs. This deformation has a vanishing energy cost due to the constant dispersion relation of the flat band. An example of momentum distributions and correlations obtained from mean-field calculations on the kagome lattice is shown in Fig. 2.4 for an FF phase involving the flat band (see the Appendix for details on the mean-field theory). There are two dominant forms of pairing: intraband pairing on the second dispersive band, and interband pairing between that band and the flat band. The former is limited to the region where the Fermi surfaces of the two components are matched. This region is quite small, as the Fermi surface shrinks when approaching the flat band singularity. Interband pairing, on the other hand, takes place in a large portion of the Brillouin zone, due to the possibility for atoms on the flat band to adjust their momentum distribution freely.

Chapter 3

Dynamical mean-field theory

Dynamical mean-field theory (DMFT) is a family of methods used to solve problems involving strongly correlated fermions [41]. It is based on the idea of replacing the original lattice model by a quantum impurity problem. Concretely, the problem is solved exactly for a small cluster, while the rest of the lattice model is treated as an effective medium.

In this chapter, we first review the concept of Green's functions, which is central in the formulation of DMFT. Then, we will explain the DMFT algorithm for single sites and clusters.

Green's functions

Let $\mathcal{D}$ be a linear differential operator acting on the coordinate $\boldsymbol{r}$, and let us consider the problem

$$\mathcal{D}\phi(\boldsymbol{r}) = \rho(\boldsymbol{r}). \tag{3.1}$$

To solve this, we introduce the Green's function $G(\boldsymbol{r})$, defined as the solution to

$$\mathcal{D}G(\boldsymbol{r}-\boldsymbol{r}') = \delta(\boldsymbol{r}-\boldsymbol{r}'). \tag{3.2}$$

Multiplying both sides of Eq. (3.2) by $\rho(\boldsymbol{r}')$, and integrating with reference to $\boldsymbol{r}'$ we get

$$\int \mathcal{D}G(\boldsymbol{r}-\boldsymbol{r}')\rho(\boldsymbol{r}')\ \mathrm{d}\boldsymbol{r}' = \int \delta(\boldsymbol{r}-\boldsymbol{r}')\rho(\boldsymbol{r}')\ \mathrm{d}\boldsymbol{r}' \tag{3.3}$$

$$\Rightarrow \mathcal{D}\left(\int G(\boldsymbol{r}-\boldsymbol{r}')\rho(\boldsymbol{r}')\right) = \rho(\boldsymbol{r}). \tag{3.4}$$

It immediately follows that

$$\phi(\boldsymbol{r}) = \int G(\boldsymbol{r} - \boldsymbol{r}')\rho(\boldsymbol{r}')\, \mathrm{d}\boldsymbol{r}' \tag{3.5}$$

is a solution to the considered differential equation. This is intuitively clear: the Green's function can be interpreted as the action of a point source at $\boldsymbol{r}'$, and the integral in Eq. (3.5) is therefore the superposition of the actions of all sources in the system.

In physics, correlators of field operators are called Green's functions, even though they do not exactly fit the mathematical definition. The functions used in DMFT are Matsubara Green's functions, defined in general as

$$G_{AB}(\tau, \tau') = -\left\langle T_\tau(A(\tau)B(\tau'))\right\rangle, \tag{3.6}$$

where A and B are operators and T_τ is the time-ordering operator in imaginary time. Imaginary time τ is related to real time by the transformation $it \to \tau$.

The relation to the mathematical definition of a Green's function is seen by considering the equation of motion for the single-particle Green's function

$$G(\nu\tau, \nu'\tau') = -\left\langle T_\tau(c_\nu(\tau)c^\dagger_{\nu'}(\tau'))\right\rangle, \tag{3.7}$$

in the non-interacting case. Here, ν is a quantum number describing the state.

The equation of motion is obtained by differentiating the Green's function with reference to imaginary time:

$$\begin{aligned}
-\frac{\partial}{\partial\tau}G &= \frac{\partial}{\partial\tau}\Big(\theta(\tau-\tau')\left\langle c_\nu(\tau)c^\dagger_{\nu'}(\tau')\right\rangle \pm \theta(\tau'-\tau)\left\langle c^\dagger_{\nu'}(\tau')c_\nu(\tau)\right\rangle\Big) && (3.8)\\
&= \delta(\tau-\tau')\Big(\left\langle c_\nu(\tau)c^\dagger_{\nu'}(\tau')\right\rangle \mp \left\langle c^\dagger_{\nu'}(\tau')c_\nu(\tau)\right\rangle\Big)\\
&\quad + \theta(\tau-\tau')\left\langle [H,c_\nu](\tau)c^\dagger_{\nu'}(\tau')\right\rangle \pm \theta(\tau'-\tau)\left\langle c^\dagger_{\nu'}(\tau')[H,c_\nu](\tau)\right\rangle && (3.9)\\
&= \delta(\tau-\tau')\left\langle [c_\nu(\tau), c^\dagger_{\nu'}(\tau)]_\mp\right\rangle + \left\langle T_\tau\Big([H,c_\nu](\tau)c^\dagger_{\nu'}(\tau')\Big)\right\rangle. && (3.10)
\end{aligned}$$

Since $[c_\nu(\tau), c^\dagger_{\nu'}(\tau')]_\mp = \delta_{\nu\nu'}\delta(\tau-\tau')$ for bosons and fermions, we get

$$-\frac{\partial}{\partial\tau}G(\nu\tau,\nu'\tau') - \left\langle T_\tau([H,c_\nu](\tau)c^\dagger_{\nu'}(\tau'))\right\rangle = \delta(\tau-\tau')\delta_{\nu\nu'}. \tag{3.11}$$

Up to the term $\left\langle T_\tau([H, c_\nu](\tau)c^\dagger_{\nu'}(\tau'))\right\rangle$, this is the mathematical definition of a Green's function.

For non-interacting Fermions, the Hamiltonian is

$$H_0 = \sum_{\nu,\nu'} t_{\nu\nu'} c^\dagger_\nu c_{\nu'}, \tag{3.12}$$

where $t_{\nu\nu'}$ is the transition amplitude from a state described by ν' to a state described by ν. In this case, the equation of motion becomes

$$-\frac{\partial}{\partial\tau}G_0(\nu\tau, \nu'\tau') - \sum_{\mu,\mu'} t_{\mu\mu'}\delta_{\nu\mu}\left\langle T_\tau(c_{\mu'}(\tau)c^\dagger_{\nu'}(\tau'))\right\rangle = \delta(\tau-\tau')\delta_{\nu\nu'} \tag{3.13}$$

$$\Rightarrow -\frac{\partial}{\partial\tau}G_0(\nu\tau, \nu'\tau') - \sum_{\nu''} t_{\nu\nu''}G_0(\nu''\tau, \nu'\tau') = \delta(\tau-\tau')\delta_{\nu\nu'}. \tag{3.14}$$

If we define a matrix G_0 such that $[G_0]_{\nu,\nu'} = G_0(\nu\tau, \nu'\tau')$, the equation of motion can be rewritten

$$G_0^{-1}G_0 = \mathbf{1}, \qquad (\partial_\tau - H) = G_0^{-1}. \tag{3.15}$$

In the Heisenberg picture, the time dependence of operators is given by $A(t) = e^{iHt}A(0)e^{-iHt}$, corresponding in imaginary time to $A(\tau) = e^{H\tau}A(0)e^{-H\tau}$. Assuming the Hamiltonian is time-independent, we can write for $\tau' > \tau$

$$\begin{aligned}
G(\nu\tau, \nu'\tau') &= -\left\langle T_\tau\big(c_\nu(\tau)c^\dagger_{\nu'}(\tau')\big)\right\rangle \\
&= \frac{1}{Z}\mathrm{Tr}[e^{-\beta H}c^\dagger_{\nu'}(\tau')c_\nu(\tau)] \\
&= \frac{1}{Z}\mathrm{Tr}[e^{-\beta H}e^{H\tau'}c^\dagger_{\nu'}(0)e^{-H\tau'}e^{H\tau}c_\nu(0)e^{-H\tau}] \\
&= \frac{1}{Z}\mathrm{Tr}[e^{-\beta H}c^\dagger_{\nu'}(0)e^{H(\tau-\tau')}c_\nu(0)e^{-H(\tau-\tau')}] \\
&= -\frac{1}{Z}\mathrm{Tr}[e^{-\beta H}T_\tau\big(c_\nu(\tau-\tau')c^\dagger_{\nu'}(0)\big)] \\
&= G(\nu[\tau-\tau'], \nu'[0])
\end{aligned} \tag{3.16}$$

The proof for $\tau > \tau'$ is similar. The Green's function therefore only depends on the imaginary time difference $\tau - \tau'$. As a consequence, we can consider only the functions $G(\nu, \nu', \tau) \equiv -\left\langle T_\tau\big(c_\nu(\tau)c^\dagger_{\nu'}(0)\big)\right\rangle$ without loss of generality. The function $G(\nu, \nu', \tau)$ is defined in the interval $-\beta < \tau < \beta$.

The Fourier transform of the Green's function can then be written as a series

$$G(n) = \frac{1}{2}\int_{-\beta}^{\beta} \mathrm{d}\tau e^{i\pi n\tau/\beta} G(\tau), \tag{3.17}$$

$$G(\tau) = \frac{1}{\beta}\sum_{n=-\infty}^{\infty} e^{-i\pi n\tau/\beta} G(n). \tag{3.18}$$

This Fourier transform can be simplified by noting that for $-\beta < \tau < 0$,

$$\begin{aligned} G(\nu,\nu',\tau) &= -\left\langle T_\tau\big(c_\nu(\tau)c^\dagger_{\nu'}(0)\big)\right\rangle \\ &= \frac{1}{Z}\mathrm{Tr}[e^{-\beta H}c^\dagger_{\nu'}(0)e^{H\tau}c_\nu(0)e^{-H\tau}] \\ &= \frac{1}{Z}\mathrm{Tr}[c^\dagger_{\nu'}(0)e^{-\beta H}e^{H(\tau+\beta)}c_\nu(0)e^{-H(\tau+\beta)}] \\ &= \frac{1}{Z}\mathrm{Tr}[e^{-\beta H}c_\nu(\tau+\beta)c^\dagger_{\nu'}(0)] \\ &= \big\langle T_\tau\big(c_\nu(\tau+\beta)c_{\nu'}(0)^\dagger\big)\big\rangle \\ &= -G(\nu,\nu',\tau+\beta). \end{aligned} \tag{3.19}$$

The proof for the case $0 < \tau$ is similar. We therefore get the translation property

$$G(\tau) = -G(\tau+\beta). \tag{3.20}$$

Using this property, the Fourier transform in Eq. (3.17) can be rewritten

$$\begin{aligned} G(n) &= \frac{1}{2}\int_0^\beta \mathrm{d}\tau e^{i\pi n\tau/\beta}G(\tau) + \frac{1}{2}\int_{-\beta}^0 \mathrm{d}\tau e^{i\pi n\tau/\beta}G(\tau) \\ &= \frac{1}{2}\int_0^\beta \mathrm{d}\tau e^{i\pi n\tau/\beta}G(\tau) + \frac{1}{2}e^{-i\pi n}\int_0^\beta \mathrm{d}\tau e^{i\pi n\tau/\beta}G(\tau-\beta) \\ &= \frac{1}{2}(1-e^{-i\pi n})\int_0^\beta \mathrm{d}\tau e^{i\pi n\tau/\beta}G(\tau). \end{aligned} \tag{3.21}$$

The factor $(1 - e^{-i\pi n})$ is zero for even n and 2 for odd n. The Fourier transform is thus for Fermions

$$G(\omega_n) = \int_0^\beta \mathrm{d}\tau e^{i\omega_n\tau}G(\tau), \tag{3.22}$$

where we have introduced the fermionic Matsubara frequencies $\omega_n = \pi(2n+1)/\beta$.

With these properties, deriving the Green's function for non-interacting fermions from the equation of motion (Eq. (3.14)) is straightforward. Noting that the imaginary time derivative corresponds to a multiplication by $i\omega_n$, we get

$$G_0(\nu,\nu',\omega_n) = (i\omega_n - t_{\nu,\nu'})^{-1}. \tag{3.23}$$

This non-interacting Green's function is related to the general Green's function through the Dyson equation

$$G(\omega_n) = (G_0(\omega_n)^{-1} - \Sigma(\omega_n))^{-1}, \tag{3.24}$$

where $\Sigma(\omega_n)$ is the self-energy.

DMFT algorithm

Real-space DMFT

The focus in this work is on superfluidity, which is conveniently studied using the Nambu formalism. The Nambu Green's function is defined as 2×2 blocks:

$$G_{ij}(\tau) = -\begin{pmatrix} \left\langle T_\tau c_{\uparrow,i}(\tau) c^\dagger_{\uparrow,j}(0)\right\rangle & \left\langle T_\tau c_{\uparrow,i}(\tau) c_{\downarrow,j}(0)\right\rangle \\ \left\langle T_\tau c^\dagger_{\downarrow,i}(\tau) c^\dagger_{\uparrow,j}(0)\right\rangle & \left\langle T_\tau c^\dagger_{\downarrow,i}(\tau) c_{\downarrow,j}(0)\right\rangle \end{pmatrix} \tag{3.25}$$

$$= \begin{pmatrix} G_{\uparrow,ij}(\tau) & F_{ij}(\tau) \\ F^\dagger_{ij}(\tau) & -G_{\downarrow,ji}(-\tau) \end{pmatrix}. \tag{3.26}$$

The indices i and j label lattice sites. The normal Green's functions are $G_{\sigma,ij}$ and F_{ij} are the anomalous ones. The latter are related to the order parameter in the following way:

$$\Delta_i = \lim_{\tau\to 0} -UF_{ii}(\tau). \tag{3.27}$$

As discussed in the previous section, the Green's function is related to the non-interacting Green's function through the Dyson equation (3.24). Using the result in Eq. (3.23), the non-interacting Green's function is written as

$$G^{-1}_{0,ij}(\omega_n) = \begin{pmatrix} i\omega_n + t_{ij} + \mu_\uparrow\delta_{ij} & 0 \\ 0 & i\omega_n - t_{ij} - \mu_\downarrow\delta_{ij} \end{pmatrix}, \tag{3.28}$$

where t_{ij} is the hopping between sites i and j. In this work, this is t for nearest neighbors and 0 otherwise.

The key approximation in DMFT is that the self-energy is local, that is $\Sigma_{ij} = \delta_{ij}\Sigma_i$. In real-space DMFT, the self-energy Σ_i is allowed to vary from site to site, which allows for the study of inhomogeneous phases. This local self-energy is solved from single-site impurity problems. In these problems, the original lattice model is mapped to a model where a single site is embedded in a bath of non-interacting orbitals representing the rest of the lattice. Particles can hop between the bath and the impurity.

More specifically, the impurity problem of site i is solved to obtain the local Green's function $\mathcal{G}_i$, given the on-site interaction strength U and the local Green's function for the bath, $\mathcal{G}_{i,\mathrm{bath}}$. The bath Green's function $\mathcal{G}_{i,\mathrm{bath}}$ is constructed by removing the self-energy of site i from G_{ii} as follows. The Neumann expansion of the Dyson equation in Eq. 3.24 is

$$G_{ij} = G_{0,ij} + \sum_{k_1} G_{0,ik_1}\Sigma_{k_1}G_{0,k_1j} + \sum_{k_1,k_2} G_{0,ik_1}\Sigma_{k_1}G_{0,k_1k_2}\Sigma_{k_2}G_{0,k_2j} + \dots, \quad (3.29)$$

where we used that $\Sigma_{nm} = \delta_{nm}\Sigma_n$. Removing Σ_i from the expression for G_{ii}, we get

$$\mathcal{G}_{i,\mathrm{bath}} = G_{0,ii} + \sum_{k_1\neq i} G_{0,ik_1}\Sigma_{k_1}G_{0,k_1i} + \sum_{k_1,k_2\neq i} G_{0,ik_1}\Sigma_{k_1}G_{0,k_1k_2}\Sigma_{k_2}G_{0,k_2i} + \dots. \quad (3.30)$$

Rewriting G_{ii} in terms of $\mathcal{G}_{i,\mathrm{bath}}$, we obtain

$$\begin{aligned} G_{ii} &= \mathcal{G}_{i,\mathrm{bath}} + \mathcal{G}_{i,\mathrm{bath}}\Sigma_i\mathcal{G}_{i,\mathrm{bath}} + \mathcal{G}_{i,\mathrm{bath}}\Sigma_i\mathcal{G}_{i,\mathrm{bath}}\Sigma_i\mathcal{G}_{i,\mathrm{bath}} + \dots && (3.31) \\ &= (\mathcal{G}_{i,\mathrm{bath}}^{-1} - \Sigma_i)^{-1} && (3.32) \\ \Rightarrow \mathcal{G}_{i,\mathrm{bath}}(\omega_n)^{-1} &= (G_{ii}(\omega_n))^{-1} + \Sigma_i(\omega_n). && (3.33) \end{aligned}$$

Once the local Green's function $\mathcal{G}_i$ is obtained, the local self-energy is computed as

$$\Sigma_{i,\mathrm{imp}}(\omega_n) = \mathcal{G}_{i,\mathrm{bath}}^{-1}(\omega_n) - \mathcal{G}_i^{-1}(\omega_n). \quad (3.34)$$

For the solution to be physically correct, we should have $G_{ii} = \mathcal{G}_i$. As is evident from equations (3.33) and (3.34), this is equivalent to having $\Sigma_{i,\mathrm{imp}} = \Sigma_i$, meaning the self-energy obtained as the result of the impurity problem should be the same as the self-energy input in the Dyson equation (3.24).

This is achieved by performing a fixed point iteration using the following algorithm:

0. Make an initial guess for the self-energy Σ_i.

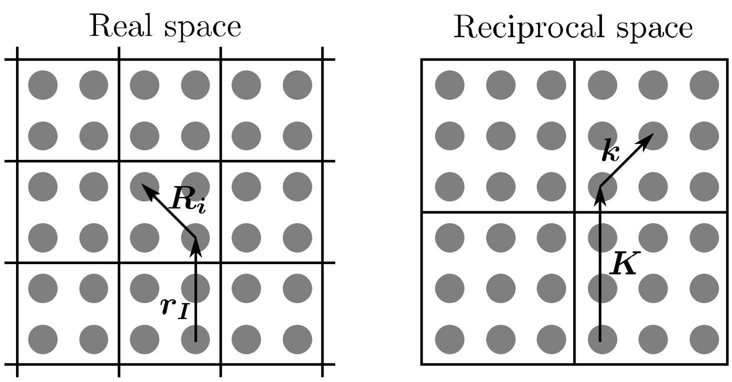

Figure 3.1: Coordinates in real space and reciprocal space for a square lattice. Black lines show the boundaries of clusters in real space and cells in reciprocal space.

1. Compute G_{ij} from Eq. (3.24).
2. Construct $\mathcal{G}_{i,\text{bath}}$ using Eq. (3.33).
3. Solve the impurity problems to obtain $\mathcal{G}_i$ at all sites.
4. Compute $\Sigma_{i,\text{imp}}$ from Eq. (3.34).
5. Check if $\Sigma_{i,\text{imp}} = \Sigma_i$ to the desired accuracy. Finish if the result has converged. Otherwise, set $\Sigma_i = \Sigma_{i,\text{imp}}$ and return to 1.

It should be noted that if the self-energy is not assumed to be translationally invariant, the impurity problems are nonequivalent at different sites. One can make the further assumption that Σ_i is the same at all sites, in which case only one impurity problem has to be solved at each iteration. In this work, we use an exact diagonalization solver and a continuous time Monte-Carlo solver to solve the impurity problem. These are discussed in Chapter 4.

Cluster extensions of DMFT

The real-space DMFT presented in the previous section assumes the self-energy is local. To include also non-local fluctuations, one needs cluster extensions of DMFT [42]. In these methods, quantum fluctuations are treated exactly not only at a single site, but in a cluster of several sites. In the limit of infinite cluster size, these methods become exact. Two examples of such extensions are cellular dynamical mean-field theory (CDMFT) [43] and dynamical cluster approximation (DCA) [44].

In these methods, the lattice is divided in clusters of N_C sites, which are unit cells possibly larger than the primitive unit cell. Correspondingly, the first Brillouin zone is divided into a set of cells. We use $\boldsymbol{r_I}$ to refer to the origins of the clusters, and $\boldsymbol{K}$ to the origins of the cells in reciprocal space. The positions of sites within a cluster with reference to its origin are $\boldsymbol{R_i}$, and positions of k points within cells in the reciprocal space are given by $\boldsymbol{k}$ (see Fig. 3.1). We assume the lattice is finite with periodic boundary conditions.

Quantities that are translationally invariant in the superlattice formed by points $\boldsymbol{r_I}$ can be Fourier transformed in the $\boldsymbol{r_I}$ coordinates to obtain an expression in reciprocal space. The Dyson equation for the full Green's function then reads

$$G(\boldsymbol{k}) = (G_0^{-1}(\boldsymbol{k}) - \Sigma)^{-1}, \tag{3.35}$$

where $G_0(\boldsymbol{k})$ is the non-interacting Green's function of the lattice model. In real-space DMFT, we assumed the self-energy was diagonal, but in cluster methods, it is assumed block-diagonal. This means that all intercluster components are neglected, but intracluster components are taken into account. Like in real-space DMFT, the self-energy block corresponding to one cluster is obtained as the solution of a quantum impurity problem.

In this case, the impurity is the cluster instead of a single site. Key elements in formulating the problem are the coarse-grained Green's function and interaction. For the impurity problem, we need to modify these quantities so that they are purely local to the cluster, which means they should be $\boldsymbol{k}$-independent. This is achieved by taking the average over the $\boldsymbol{k}$ points:

$$\overline{G} = \frac{1}{N_k} \sum_{\boldsymbol{k}} G(\boldsymbol{k}), \tag{3.36}$$

and similarly for the interaction matrix. Here, N_k is the number of $\boldsymbol{k}$ points, or equivalently, the number of clusters in the lattice. More explicitely,

$$\overline{G}(\omega_n) = \frac{1}{N_k} \sum_{\boldsymbol{k}} (i\omega_n - t_{\boldsymbol{k}} - \Sigma(\omega_n))^{-1}, \tag{3.37}$$

where $t_{\boldsymbol{k}}$ is the Fourier transform of the hopping matrix. The difference between DCA and CDMFT is in how this Fourier transform is calculated. In CDMFT,

$$t_{\boldsymbol{k}} = \sum_I t_{0I} \exp(i\boldsymbol{k} \cdot (\boldsymbol{r}_0 - \boldsymbol{r}_I)), \tag{3.38}$$

where t_{0I} is the hopping matrix between clusters 0 and I. For DCA,

$$t_{\boldsymbol{k},ij} = \sum_I t_{0I,ij} \exp(i\boldsymbol{k} \cdot (\boldsymbol{r}_0 - \boldsymbol{r}_I + \boldsymbol{R}_i - \boldsymbol{R}_j)), \tag{3.39}$$

where $t_{0I,ij}$ is the hopping amplitude between site i of cluster 0 and site j of cluster I. The Fourier transformation used in CDMFT breaks the translational invariance within the cluster, whereas the one used in DCA does not. CDMFT may therefore overestimate the stability of non-uniform phases. It should also be noted that the hopping matrix in DCA depends also on the intracluster coordinates. This means that the coarse-grained Green's function depends on the momentum $\boldsymbol{K}$ in reciprocal space.

The bath Green's function for the impurity problem can be computed from the coarse-grained Green's function in a way similar to what is done in real-space DMFT:

$$\mathcal{G}_{\text{bath}} = (\overline{G}^{-1}(\omega_n) + \Sigma(\omega_n))^{-1}. \tag{3.40}$$

Note that in DCA, since $\overline{G}$ depends on $\boldsymbol{K}$, also the self-energy depends on $\boldsymbol{K}$. Solving the impurity problem for the self-energy closes the self-consistency loop.

Based on the cluster DMFT formalism, it is possible to formulate a partially real-space DMFT. The idea is to split the cluster in subclusters. The self-energy is then approximated to be block-diagonal so that the components between subclusters are neglected. An impurity problem is then solved for each subcluster.

FFLO states in DMFT

As explained in Sec. 2.3, FFLO states are such that the order parameter is modulated in real space. To study such states, one possibility is to consider large clusters with the possibility for a space-dependent order parameter. However, this usually requires large cluster sizes, which demand prohibitively long computation times when using cluster DMFT. In this case, real-space or partially real-space DMFT is better suited. It has indeed been used to study the FFLO phase in the 1D-3D crossover [45] and the striped phase in the repulsive Hubbard model [46]. The latter is related to the FFLO phase in particle-hole symmetric systems: the striped phase in the repulsive Hubbard model corresponds to the FFLO state in the attractive Hubbard model.

Another option to study FF phases without having to consider large clusters is presented below. The principle is to perform a transformation on the creation and annihilation operators that cancels the momentum dependence of the order parameter in the FF ansatz, $\Delta_i = U \langle c_{\uparrow,i} c_{\downarrow,i} \rangle = \Delta_{\alpha_i} e^{i\boldsymbol{q}\cdot\mathbf{r}_i}$, where α_i designates the Bravais sublattice of lattice site i. There are many equivalent transformations that achieve this, for example $c^\dagger_{\uparrow,i} \to e^{i\boldsymbol{q}\cdot\mathbf{r_i}} c^\dagger_{\uparrow,i}$ and $c_{c_{\uparrow,i}} \to e^{-i\boldsymbol{q}\cdot\mathbf{r_i}} c_{\uparrow,i}$, where $\boldsymbol{q}$ is the Cooper pair quasimomentum. As a result of this transformation, $\left\langle c^\dagger_{\uparrow,i} c_{\uparrow,j} \right\rangle$ becomes $\left\langle c^\dagger_{\uparrow,i} c_{\uparrow,j} \right\rangle e^{i\boldsymbol{q}\cdot(\mathbf{r_i}-\mathbf{r_j})}$. Effectively, this modifies the hopping amplitudes between sites: t_{ij} is replaced by $\tilde{t}_{ij} = t_{ij} e^{i\boldsymbol{q}\cdot(\boldsymbol{r_i}-\boldsymbol{r_j})}$.

A system with hopping amplitudes t_{ij} where the ground state has order parameters $\Delta_i = \Delta_{\alpha_i} e^{i\boldsymbol{q}\cdot\mathbf{r_i}}$ is thus equivalent to a system with hopping amplitudes $\tilde{t}_{ij}$ where the order parameters in the ground state are $\Delta_i = \Delta_{\alpha_i}$. Note that in the latter case, the order parameter can be different between sublattices, but does not vary otherwise. This makes it possible to study the FF state with cluster DMFT using the primitive unit cell as a cluster. This is typically much smaller than what would be needed to study an FFLO state using the previously mentioned method.

To determine whether the FF state is the ground state, one has to perform a DMFT computation for different quasimomenta $\boldsymbol{q}$, each one for a lattice model with hopping amplitudes $\tilde{t}_{ij}$. The thermodynamic potential of the states obtained as a result of these computations is compared to determine which one is the ground state. If this ground state occurs at $\boldsymbol{q} \neq 0$ with at least one order parameter $\Delta_\alpha \neq 0$, the ground state is an FF state.

One shortcoming of this method is that it requires the assumption that the state is indeed an FF state, as opposed to a more complicated FFLO state. In real-space DMFT, such states should naturally arise if they are the ground state. However, considering the FF state can give a good picture of the stability region of FFLO states even when the ansatz does not correspond to the true ground state [40]. Another issue is the necessity to perform the DMFT computation separately for different $\boldsymbol{q}$. In practice, considering all possible values in the irreducible Brillouin zone is cumbersome, and some educated guess on the direction of $\boldsymbol{q}$ can be needed. Finding a very precise value for $\boldsymbol{q}$ can also be difficult. However, the method can still give information on the possible stability of the FF state, even if the exact quasimomentum is not known.

The advantage is that a cluster equal to the irreducible unit cell is sufficient. In the kagome lattice, this corresponds to only three lattice sites. At this cluster size, it is possible to fully take into account the quantum fluctuations in the cluster. Moreover, the computation time is much shorter than for the larger unit cells needed to study other FFLO states.

Chapter 4

Impurity solvers

In this chapter, we briefly present the two impurity solvers used in this work. The first one is an exact diagonalization solver, which can be used at zero and low temperatures. The second is a continuous time Monte-Carlo solver based on an iteraction expansion (CT-INT), which is more appropriate for higher temperatures.

Exact diagonalization

Exact diagonalization is a method used to calculate the Green function of a cluster by representing the impurity problem with a Hamiltonian acting on a finite-dimensional Hilbert space, which is then diagonalized [47–49]. The initial impurity problem has an infinite number of degrees of freedom, so the first step in exact diagonalization is to fit a model with a finite number of orbitals to the impurity model.

The impurity has a finite number of orbitals n_i, so the problem is to discretize the bath to represent it by a finite number n_b of orbitals. The kinetic term in the Hamiltonian of the discretized system should have the form

$$H_{\text{kin}} = \begin{pmatrix} T_{\text{i}} & V^{\dagger} \\ V & T_{\text{b}} \end{pmatrix}, \tag{4.1}$$

where T_{i} is a $n_i \times n_i$ block containing the hopping parameters between the impurity orbitals, T_{b} is a $n_b \times n_b$ block containing those between the bath orbitals, and V is a $n_b \times n_i$ block containing hopping parameters between the impurity and bath. Note that T_{b} can always be chosen to be diagonal: as it is Hermitian, we can perform a unitary trasformation that diagonalizes the block.

The bath Green function $\mathcal{G}_{\mathrm{bath}}$ is equal to the non-interacting Green function of the impurity, $\mathcal{G}_{0,\mathrm{i}}$. The fitting procedure is therefore done by demanding that the Green function $\tilde{\mathcal{G}}_{0,\mathrm{i}}$ corresponding to the Hamiltonian (4.1) is as close as possible to $\mathcal{G}_{0,\mathrm{i}}$. Explicitely, $\tilde{\mathcal{G}}_{0,\mathrm{i}}$ is given by the upper left $n_i \times n_i$ block of the full non-interacting Green function,

$$\tilde{\mathcal{G}}_{0,\mathrm{i}}(\omega_n) = \left[(i\omega_n - H_{\mathrm{kin}})^{-1}\right]_{1\ldots n_i, 1\ldots n_i}. \tag{4.2}$$

The fitting is done by minimizing a cost function describing the "distance" between $\tilde{\mathcal{G}}_{0,\mathrm{i}}$ and $\mathcal{G}_{0,\mathrm{i}} = \mathcal{G}_{\mathrm{bath}}$, with T_{i}, T_{b} and V as the fitting parameters [50].

Once the fitting is done, the full Hamiltonian matrix H can be constructed. A basis of the Hilbert space of H is given by

$$|n_1^{\uparrow}, n_2^{\uparrow}, \ldots, n_{n_i+n_b}^{\uparrow}\rangle |n_1^{\downarrow}, n_2^{\downarrow}, \ldots, n_{n_i+n_b}^{\downarrow}\rangle, \tag{4.3}$$

where $n_i^{\sigma} = 0$ or 1 is the number of particles with spin σ at site i. Often H is block diagonal, as the number of particles of each component is conserved. In this case, the Hilbert space is divided in subspaces described by the total number of particles of each spin, $(n^{\uparrow}, n^{\downarrow})$. Each corresponding block can be diagonalized independently. However, in the superfluid phase, the conservation of components no longer holds, so the size of the problem cannot generally be reduced.

If the matrix is small enough, all eigenstates and eigenvalues can be solved. The Green's function can then be calculated at finite temperatures from them [48]. If the matrix is too large, however, it is still possible to study the zero-temperature case by using a Lanczos algorithm [48, 51]. Even using this method, exact diagonalization is limited to a quite small number of sites. However, this solver has the advantage to make it possible to study low temperatures and the zero-temperature case. Moreover, the method has no sign problem, contrary to quantum Monte-Carlo methods.

Continuous time Monte-Carlo solver

Metropolis Monte Carlo

The Monte Carlo method is used to compute sums of the form $\sum_x p(x)f(x)$, where p is a probability distribution. The idea is to replace the sum by an average over a set $\{x_i\}$ of stochastically generated configurations such that the probability of getting x_n is $p(x_n)$.

The set is generated as a Markov chain, that is, a sequence where the transition probabilities towards other configurations depend only on the current configuration. If p is the equilibrium distribution of the Markov chain, the chain will converge to it provided it is ergodic, meaning all states can be reached, and that the transition rates satisfy the balance condition $\sum_{y:y\neq x} p(y)w_{y,x} = \sum_{y:y\neq x} p(x)w_{x,y}$. Here, $w_{y,x}$ is the transition probability in the Markov chain to go from y to x. This is often replaced by the stricter condition

$$\frac{w_{x,y}}{w_{y,x}} = \frac{p(y)}{p(x)}. \tag{4.4}$$

Generating the Markov chain is commonly achieved with the Metropolis-Hastings algorithm. In this algorithm, a change to configuration y is proposed with some probability $P_{x,y}$. The proposal is then accepted with probability $A_{x,y}$. Otherwise, the configuration is left the same. Then the total transition rate from x to y is $w_{x,y} = A_{x,y}P_{x,y}$. Defining the acceptance probability as

$$A_{x,y} = \min\left(1, \frac{P_{y,x}p(y)}{P_{x,y}p(x)}\right), \tag{4.5}$$

we obtain a transition rate $w_{x,y}$ that satisfies the conditions given above.

Interaction expansion

We consider the Hubbard model

$$H = H_0 + H_{\text{int}} = -\sum_{i,j,\sigma} t_{i,j} c^\dagger_{\sigma,i} c_{\sigma,j} + U\sum_i (n_{\uparrow,i} - 1/2)(n_{\downarrow,i} - 1/2). \tag{4.6}$$

The interaction term can be rewritten as

$$H_{\text{int}} = \frac{U}{2}\sum_i \sum_{s=\pm 1} (n_{\uparrow,i} - 1/2 - s\delta)(n_{\downarrow,i} - 1/2 + s\delta). \tag{4.7}$$

This corresponds to adding a constant $U\delta^2$, which has no physical meaning. However, the introduction of δ will be helpful for solving sign problems.

In this work, we use a method based on a weak-coupling expansion of the partition function (CT-INT). This expansion takes the form [52]

$$\frac{Z}{Z_0} = \sum_{C_n} W(C_n), \tag{4.8}$$

with

$$Z_0 = \mathrm{Tr}[e^{-\beta H_0}] \tag{4.9}$$

$$W(C_n) = \left(-\frac{U}{2}\right)^n \frac{1}{n!} \prod_\sigma \det M_\sigma(C_n), \tag{4.10}$$

$$\sum_{C_n} = \sum_{n=0}^{\infty} \int_0^\beta \mathrm{d}\tau_1 \sum_{i_1,s_1} \cdots \int_0^\beta \mathrm{d}\tau_n \sum_{i_n,s_n}, \tag{4.11}$$

$$M_\sigma(C_n) = \begin{pmatrix} G^0_{i_1,i_1}(\tau_1,\tau_1) - \alpha_\sigma(s_1) & G^0_{i_1,i_2}(\tau_1,\tau_2) & \dots & G^0_{i_1,i_n}(\tau_1,\tau_n) \\ G^0_{i_2,i_1}(\tau_2,\tau_1) & G^0_{i_2,i_2}(\tau_2,\tau_2) - \alpha_\sigma(s_2) & \dots & G^0_{i_2,i_n}(\tau_2,\tau_n) \\ \vdots & \vdots & \vdots & \vdots \\ G^0_{i_n,i_1}(\tau_n,\tau_1) & G^0_{i_n,i_2}(\tau_n,\tau_2) & \dots & G^0_{i_n,i_n}(\tau_n,\tau_n) - \alpha_\sigma(s_n) \end{pmatrix}, \tag{4.12}$$

$$\alpha_\sigma(s) = 1/2 + \sigma s \delta. \tag{4.13}$$

The functions $G^0_{i,j}$ are the Green functions $G^0_{i,j}(\tau_1,\tau_2) = \left\langle T c_i^\dagger(\tau_1) c_j(\tau_2) \right\rangle_0$, with $\langle \bullet \rangle_0 = \mathrm{Tr}[e^{-\beta H_0} \bullet]$.

These give the expression for the weigths $W(C_n)$ of the configurations $C_n = \{[i_1,\tau_1,s_1] \dots [i_n,\tau_n,s_n]\}$. In the metropolis Monte Carlo algorithm, the proposed updates to the configuration C_n are the additions and removals of vertices of the form $[i,\tau,s]$ to or from the list C_n.

Expectation vaues of observables $O(\tau)$ can then be computed as an average

$$\langle O(\tau) \rangle = \frac{\sum_{C_n} W(C_n) \langle\langle O(\tau) \rangle\rangle_{C_n}}{\sum_{C_n} W(C_n)}, \tag{4.14}$$

where

$$\langle\langle O(\tau) \rangle\rangle_{C_n} = \frac{\prod_\sigma \langle T[n_{i_1,\sigma}(\tau_1) - \alpha_\sigma(s_1)] \dots [n_{i_n,\sigma}(\tau_n) - \alpha_\sigma(s_n)] O_\sigma(\tau) \rangle_0}{\prod_\sigma \langle T[n_{i_1,\sigma}(\tau_1) - \alpha_\sigma(s_1)] \dots [n_{i_n,\sigma}(\tau_n) - \alpha_\sigma(s_n)] \rangle_0} \tag{4.15}$$

With this impurity solver, there can be a sign problem, which occurs when configurations with negative weight appear. From Eq. (4.10), it is clear this happens when the sign of $\prod_\sigma \det M_\sigma(C_n)$ has a sign different from $(-U/2)^n$. This sign can be changed by tuning δ. For example in one dimension, the sign problem is removed by setting $\delta > 1/2$.

Chapter 5

Results

Critical temperature

Before studying the FFLO state, we first present the critical temperatures at different interactions given by DMFT calculations in Fig. 5.1. For these calculations, we used the three-site unit cell as a cluster, and restricted to the balanced case $h = (\mu_\uparrow - \mu_\downarrow)/2 = 0$. The impurity solver used here is the CT-INT solver, as it allows to study non-zero temperatures. Moreover, the sign problem does not occur in the balanced case.

As can be seen from the results, the critical temperature obtained from DMFT calculations is lower than the one obtained from mean-field calculations. This is not surprising: mean-field theories typically overestimate the critical temperature, as fluctuations are neglected. With increasing interaction, the difference becomes more pronounced: for fillings near the flat band, the mean-field critical temperature is about twice the DMFT critical temperature at $U = -2t$, but is more than three times larger at interaction $U = -4t$.

Table 5.1: Ratio $T_{C,\mathrm{MF}}/T_{C,\mathrm{DMFT}}$ for different fillings and interactions.

	$f \approx 0.2$	$f \approx 0.7$
$U = -2t$	2.2	2.2
$U = -3t$	2.1	2.6
$U = -4t$	2.7	3.1

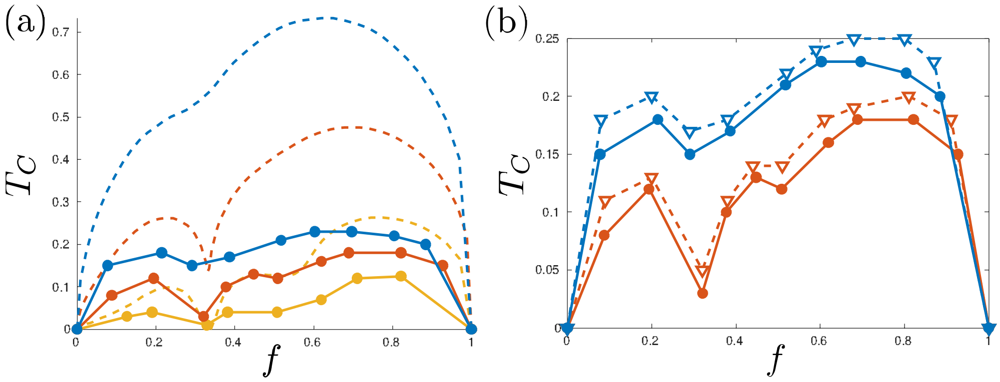

Figure 5.1: (a) Critical temperature at interactions $U = -2t$ (yellow), $U = -3t$ (red) and $U = -4t$ (blue). Connected points show cluster DMFT results, while dashed lines show mean-field results. (b) Comparison of cluster DMFT and partially real-space DMFT results at interaction strengths $U = -3t$ and $U = -4t$. Colors are the same as in (a). The cluster DMFT results are indicated by connected points, and real-space DMFT results are plotted with connected triangles.

Even though the critical temperature in DMFT is lower than in mean-field theory, it presents the same features. There is a dip at filling $f = (n_\uparrow + n_\downarrow)/2 = 1/3$, which corresponds to the filling where the density of states at the Fermi surface vanishes due to the Dirac cones in the dispersion relation. The largest critical temperature is found for fillings above 2/3, where the flat band is reached. Two maxima are found near the Van Hove singularities at $f = 1/3 \pm 1/12$. However, the difference of DMFT results compared with the mean-field ones depends on filling. In Table 5.1, we present the ratio of the mean-field critical temperature $T_{C,\mathrm{MF}}$ with the DMFT critical temperature $T_{C,\mathrm{DMFT}}$. The difference is larger for fillings near the flat band than it is at fillings on the dispersive bands. Fluctuations therefore seem to be more important to the physics near the flat band.

To know how important nonlocal fluctuations are, it is instructive to compare the critical temperature obtained above using cluster DMFT with those computed with a partially real-space DMFT. In Fig. 5.1, we show both. In the partially real-space DMFT, the three-site cluster is divided in single-site subclusters, and only quantum fluctuations local to each site are taken into account. This approximation leads to a slight overestimation of the critical temperature, but the behavior is essentially the same.

FF state

In this section, we will present results regarding the FF state. The results were obtained using the method described in Sec. 3.3: the momentum dependence of the order parameter was moved to the hopping matrices through a unitary transformation. The computation was then performed for different momenta $\boldsymbol{q}$, tuning the chemical potentials to reach the same filling fractions for all momenta. The direction of $\boldsymbol{q}$ is fixed along the axis perpendicular to $\mathbf{a}_1$, as this is the direction that is the most favorable in mean-field theory. We refer to this direction as the y axis. Here, we use an exact diagonalization (ED) solver, and consider zero temperature. Since we compare results at fixed filling fractions, we are effectively considering the canonical ensemble, and the ground state is the one with the lowest Helmholtz free energy. At zero temperature, this corresponds to the total energy.

Since the FF regions can be small, the phase can be difficult to find if one considers the whole parameter space. Mean-field results can give an indication to the regions where it is most likely to be found. In the kagome lattice, our mean-field results predict two major regions [14]. One is located around the crossing point of a flat band singularity and a Van Hove singularity, and the other is at the crossing point of two Van Hove singularities. Out of these two, the former seems to be the most robust, as it is the only one found at small interaction strengths and higher temperatures. Physically, this is probably explained by the unconventional pairing mechanism in the presence of a flat band, explained in Sec. 2.3. We therefore focus on this region in the following calculations.

Near the flat band, the iteration has a tendency to converge to a state with either a filled or empty flat band. The convergence can also be affected by the flat band, since small changes in the chemical potential can lead to large changes in the density, and thus for example the Hartree energy can cause problems. To help convergence to filling fractions between 2/3 and 1, we add a "tunable field" to the iteration. This is a diagonal matrix added to the hopping matrix which is fitted to the constant part of the self-energy. The contribution of this tunable field to the total energy is removed from the final result.

The total energy and order parameters are shown as a function of $\boldsymbol{q}$ in Fig. 5.2 for different filling fractions. As can be seen from the figures, the FF phase is indeed found, as the smallest total energy is found for states with $\boldsymbol{q} \neq 0$ and $\Delta_\alpha \neq 0$. At both FF points, $\Delta_A = \Delta_B \neq \Delta_C$. This is due to the finite

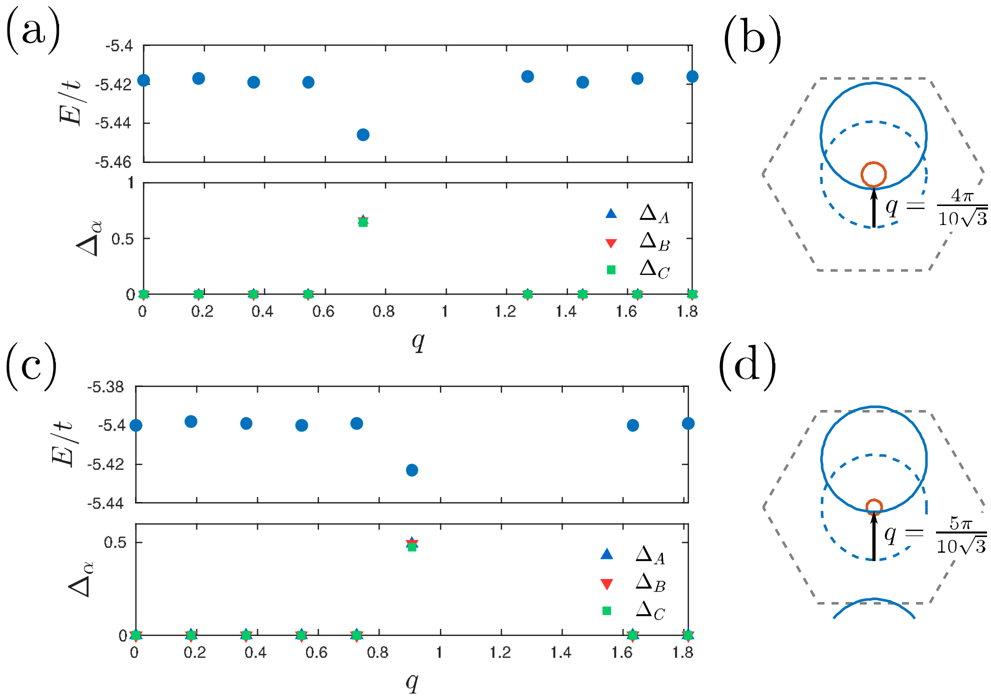

Figure 5.2: Total energy per unit cell (upper panel) and order parameters (lower panel) for different q, at filling fractions $f = (n_\uparrow + n_\downarrow)/2 = 0.619$ and $p = (n_\uparrow - n_\downarrow)/2 = 0.043$ in (a) and $f = 0.621$ and $p = 0.044$ in (c). The interaction strength is $U = -5t$. (b) and (d) show the Fermi surfaces in the non-interacting case at the same filling fractions as the DMFT calculations, one of them being shifted by the momentum found in the FF phase. The red and blue lines indicate the majority and minority Fermi surfaces, respectively. The blue dashed line shows the position of the minority Fermi surface before the shift, and gray dashed lines correspond to the boundary of the first Brillouin zone.

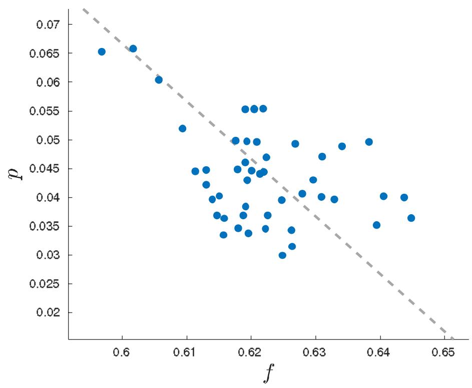

Figure 5.3: Points at which an FF phase with energy lower than the normal state was found. The dashed line indicates the parameters for which the majority component reaches the flat band. The interaction strength is $U = -5t$.

momentum $\boldsymbol{q}$: when it is perpendicular to $\mathbf{a}_1$, sites A and B are equivalent, but C is different. The difference is however quite small, which is likely explained by the small magnitude of $\boldsymbol{q}$.

The momentum at which the FF state was found is quite close to $k^y_{\mathrm{F},\uparrow} - k^y_{\mathrm{F},\downarrow}$, where $k_{\mathrm{F},\sigma}$ is the Fermi momentum for spin σ on the y axis (see Fig. 5.2), meaning the momentum is such that it connects the two Fermi surfaces. This is an indication that the conventional pairing mechanism explained in Sec. 2.3 plays a role in the formation of the FF state. The iteration did not converge properly for $\boldsymbol{q}$ near these momenta, so it is not certain that the found state is indeed the ground state. However, the reason for bad convergence may be that those values of $\boldsymbol{q}$ are unfavorable for the FF state, exactly because they do not allow to match the Fermi surfaces properly. The energy would then be closer to that of the normal state, which can impact convergence.

One feature that was not found in this study, but present at the mean-field level, is the η phase. This is an extreme version of the FF phase, where the quasimomentum is saturated at the edge of the Brillouin zone. The reason it does not appear here is probably that the FF region is at lower polarizations than those predicted by the mean-field theory. The size difference of the Fermi surfaces is not as large, so the momenta are correspondingly smaller.

Studying the momentum distributions is difficult with DMFT, as one would need to consider large clusters to obtain a good resolution. For example, DCA allows to compute quantities in reciprocal space, but the number of

k points is the number of lattice sites in the cluster [44]. A more realistic option to include the momentum-dependence of the self energy is to use a method that combines DMFT with a method that can describe the momentum dependence, such as the fluctuation-exchange (FLEX) approximation [53], the dynamical vertex approximation (DΓA) [54] or the dual Fermion approach [55]. The implementation of these methods is outside of the scope of this thesis, so we do not directly check whether the momentum distribution deformation observed at the mean-field level occurs here. However, the FF state was found at several points near the flat band singularity, as is shown in Fig. 5.3. This confirms the mean-field result that the vicinity of the flat band singularity is favorable to the stability of the FF state. Moreover, the matched region of the Fermi surfaces is small, as the Fermi surface of the majority component shrinks near the flat band. This indicates another pairing mechanism than the conventional matching of the surfaces, such as momentum distribution deformation, probably plays a role.

Real-space DMFT

The method used in the previous section requires the assumption that the FF ansatz is representative of the ground state. If the FFLO state has any more than one wave vector $\boldsymbol{q}$, it becomes impossible to use, as the $\boldsymbol{q}$ dependence cannot be transferred to the hopping matrices anymore. However, it has been shown before that the LO ansatz with two opposite wave vectors $\boldsymbol{q}$ is more favorable than the FF ansatz, for example in the square lattice [40]. It is therefore interesting to study the FFLO phase using real-space DMFT, which allows for FFLO phases more complicated than the simple FF phase.

Computations were performed for the 18 site unit cell shown in Fig. 5.4. The self-energy was assumed local within the unit cell, and translationally invariant in the superlattice of the enlarged unit cells. It is usually better to choose the unit cell so that it has the same symmetries as the original lattice [42]. However, to study FFLO states, the unit cell needs to be large enough that the modulations can fit within, at least in one dimension. Choosing a long cluster like the one used here keeps the number of lattice sites relatively small while fulfilling this condition.

As the impurity solver, we used CT-INT, with temperature $T = 1/20$. While the sign problem does not appear in the balanced attractive Hubbard model, it can occur when polarization is introduced. We thus set δ to 0.6, which solves the sign problem for single-site impurity problems [52].

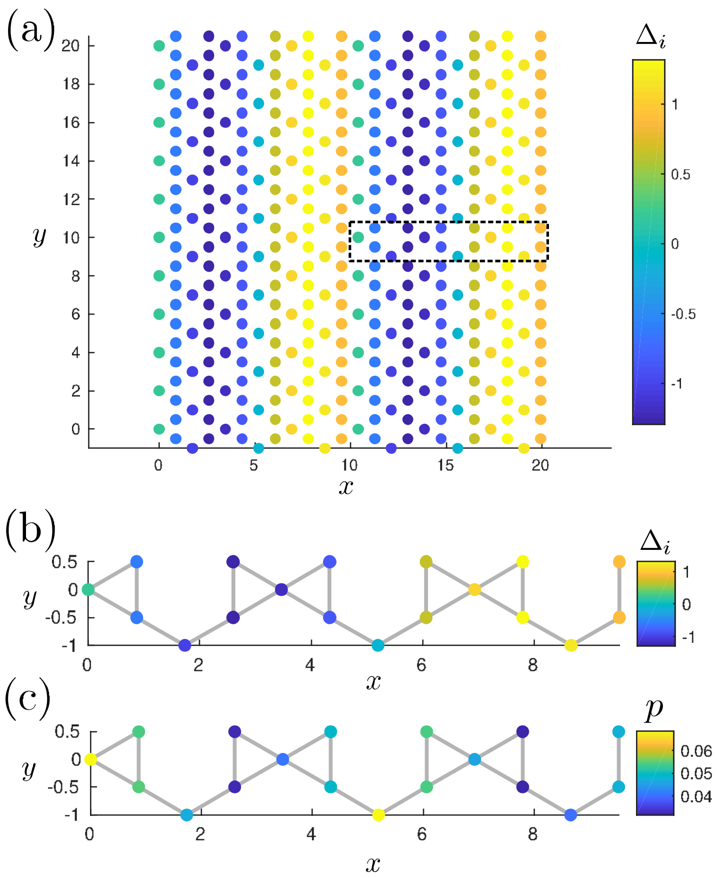

Figure 5.4: (a) Real-space dependence of the order parameter Δ_i. The computation was performed for the 18-site enlarged unit cell indicated by the dashed rectangle. The figure is obtained by stacking the unit cell in x and y direction. (b) Order parameter and (c) polarization $p = (n_\uparrow - n_\downarrow)/2$ dependence in the enlarged unit cell. The density is $f = 0.612$ and the polarization is 0.0469.

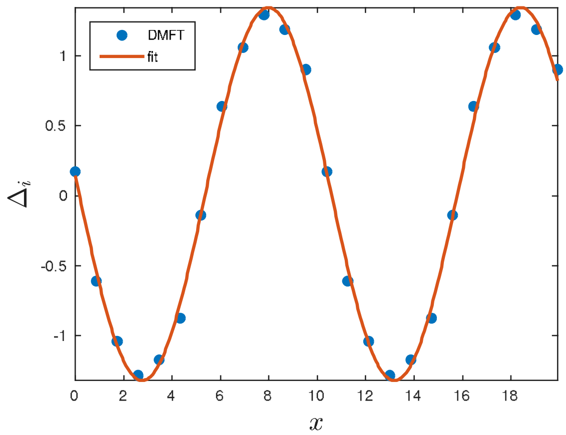

Figure 5.5: Order parameter Δ_i along the y direction, and least-squares fit of the sinusoidal function $f(y) = a\sin(2\pi\nu y + \phi) + c$, where a, ν, ϕ and c are the fitting parameters. The obtained parameters are $a = -1.33$, $\nu = 9.60 \cdot 10^{-2}$, $\phi = -9.79 \cdot 10^{-2}$ and $c = 1.18 \cdot 10^{-2}$.

The results for the order parameter and polarization are shown in Fig. 5.4. The order parameter shows clear modulations, characteristic of an FFLO type phase. These modulations are accompanied by modulations in the particle densities at the lattice sites, as is manifest from the polarizations at different sites. Where the order parameter is zero, the polarization reaches a maximum. The modulation period is the same as that for the absolute value of the order parameter. This is a feature found in the LO state.

In fact, the modulation of the order parameter is very close to sinusoidal, as can be seen from Fig. 5.5. The direction of $\boldsymbol{q}$ is along the y-axis, which is the same as the one obtained in mean-field calculations, and was assumed in the previous subsection. The amplitude of the quasimomentum obtained from the fitting is $q = 2\pi \cdot 0.0960 \approx 0.603$. The same way as in the previous section, this corresponds to the momentum that joins the Fermi surfaces in the non-interacting case.

The effect of the shape of the unit cell should however be kept in mind. If the true ground state was for example one with order parameter $\Delta = |\Delta|(\cos(\boldsymbol{q}_1 \cdot \boldsymbol{x}) + \cos(\boldsymbol{q}_2 \cdot \boldsymbol{y}))$, it would likely not appear with the unit cell used here. The reason is that for the modulation to fit in the x direction, the sign of the order parameter would need to change from site to site in that direction. This requires a quasimomentum $\boldsymbol{q}_2$ at the boundary of the

Brillouin zone, which is not likely to happen for low polarizations if the Fermi surfaces are to be matched.

The filling fraction and polarization correspond quite well to the ones found for the FF state in the previous section, giving further confirmation that FFLO states can be stable near the flat band singularity. This result is also at finite temperature, showing the stability is not an effect only found at zero temperature.

Chapter 6

Conclusions

We studied the stability of FFLO states in the Kagome lattice using DMFT. We used two different approaches: one based on a unitary transformation allowing us to include the FF ansatz in the hopping matrices instead of the order parameters, and a partially real-space approach.

The former method fully took into account the quantum fluctuations in the three-site unit cell used as a cluster. It gave a region of stable FF state in the vicinity of the flat band singularity, confirming the mean-field prediction. Even though mean-field theory overestimates the critical temperature more in that region, indicating that fluctuations are particularly important, the FFLO state is stable. This was further confirmed by the partially real-space calculation at non-zero temperature, which gave an LO type state.

The momentum in both computations was close to the difference between Fermi momenta of the two components, meaning it allowed to match the surfaces. This is a strong indication that the conventional mechanism for the formation of FFLO is present.

It should be noted that at the FFLO points found with both methods, the Fermi surfaces are nearly spherical, so Fermi surface nesting does not play a role in stabilizing the FFLO. Instead, the momentum distribution deformation of particles on the flat band probably favors the FFLO state, as the state was found in the vicinity of the singularity. To verify this effect does indeed take place also beyond mean-field level, a method that takes long-range fluctuations should be used.

The results in this work confirms that the kagome lattice can be a good candidate for a direct observation of FFLO states. The kagome lattice has already been realized experimentally for bosonic ultracold atoms [56].

Bibliography

[1] J. Bardeen, L. N. Cooper, and J. R. Schrieffer. Theory of superconductivity. *Phys. Rev.*, 108:1175–1204, Dec 1957.

[2] Leon N. Cooper. Bound electron pairs in a degenerate fermi gas. *Phys. Rev.*, 104:1189–1190, Nov 1956.

[3] M. W. Zwierlein, A. Schirotzek, C. H. Schunck, and W. Ketterle. Fermionic superfluidity with imbalanced spin populations. *Science*, 311(5760):492–496, 2006.

[4] G. B. Partridge, W. Li, R. I. Kamar, Y. Liao, and R. G. Hulet. Pairing and phase separation in a polarized fermi gas. *Science*, 311(5760):503–505, 2006.

[5] G. B. Partridge, W. Li, Y. A. Liao, R. G. Hulet, M. Haque, and H. T. C. Stoof. Deformation of a trapped fermi gas with unequal spin populations. *Phys. Rev. Lett.*, 97:190407, Nov 2006.

[6] S. Nascimbène, N. Navon, K. J. Jiang, L. Tarruell, M. Teichmann, J. McKeever, F. Chevy, and C. Salomon. Collective oscillations of an imbalanced fermi gas: Axial compression modes and polaron effective mass. *Phys. Rev. Lett.*, 103:170402, Oct 2009.

[7] P. Fulde and R. A. Ferrell. Superconductivity in a strong spin-exchange field. *Phys. Rev.*, 135:A550–A563, Aug 1964.

[8] A.I. Larkin and Y.N. Ovchinnikov. Inhomogeneous state of superconductors. *J. Exp. Theor. Phys.*, 47, 1964. cited By 11.

[9] C. Cho, J. H. Yang, N. F. Q. Yuan, J. Shen, T. Wolf, and R. Lortz. Thermodynamic evidence for the Fulde-Ferrell-Larkin-Ovchinnikov state in the KFe_2As_2 superconductor. *Phys. Rev. Lett.*, 119:217002, Nov 2017.

[10] R. Casalbuoni and G. Nardulli. Inhomogeneous superconductivity in condensed matter and qcd. *Rev. Mod. Phys.*, 76:263–320, Feb 2004.

[11] Y. Liao, A. S. C. Rittner, T. Paprotta, W. Li, G. B. Partridge, R. G. Hulet, S. K. Baur, and E. J. Mueller. Spin-imbalance in a one-dimensional fermi gas. *Nature*, 467:567 EP –, Sep 2010.

[12] T. K. Koponen, T. Paananen, J.-P. Martikainen, and P. Törmä. Finite-temperature phase diagram of a polarized Fermi gas in an optical lattice. *Phys. Rev. Lett.*, 99:120403, Sep 2007.

[13] J. J. Kinnunen, J. E. Baarsma, J.-P. Martikainen, and P. Törmä. The Fulde–Ferrell–Larkin–Ovchinnikov state for ultracold fermions in lattice and harmonic potentials: a review. *Reports on Progress in Physics*, 81(4):046401, 2018.

[14] K.-E. Huhtinen, M. Tylutki, P. Kumar, T. I. Vanhala, S. Peotta, and P. Törmä. Spin-imbalanced pairing and Fermi surface deformation in flat bands. *Phys. Rev. B*, 97:214503, Jun 2018.

[15] J. Wang, Y. Che, L. Zhang, and Q. Chen. Instability of Fulde-Ferrell-Larkin-Ovchinnikov states in atomic Fermi gases in three and two dimensions. *Phys. Rev. B*, 97:134513, Apr 2018.

[16] S. Yin, J.-P. Martikainen, and P. Törmä. Fulde-ferrell states and berezinskii-kosterlitz-thouless phase transition in two-dimensional imbalanced fermi gases. *Phys. Rev. B*, 89:014507, Jan 2014.

[17] M. O. J. Heikkinen, D.-H. Kim, and P. Törmä. Finite-temperature stability and dimensional crossover of exotic superfluidity in lattices. *Phys. Rev. B*, 87:224513, Jun 2013.

[18] D.-H. Kim, J. J. Kinnunen, J.-P. Martikainen, and P. Törmä. Exotic superfluid states of lattice fermions in elongated traps. *Phys. Rev. Lett.*, 106:095301, Feb 2011.

[19] M. O. J. Heikkinen, D.-H. Kim, M. Troyer, and P. Törmä. Nonlocal quantum fluctuations and fermionic superfluidity in the imbalanced attractive Hubbard model. *Phys. Rev. Lett.*, 113:185301, Oct 2014.

[20] J. Gukelberger, S. Lienert, E. Kozik, L. Pollet, and M. Troyer. Fulde-Ferrell-Larkin-Ovchinnikov pairing as leading instability on the square lattice. *Phys. Rev. B*, 94:075157, Aug 2016.

[21] M. J. Wolak, B. Grémaud, R. T. Scalettar, and G. G. Batrouni. Pairing in a two-dimensional Fermi gas with population imbalance. *Phys. Rev. A*, 86:023630, Aug 2012.

[22] M. Karmakar and P. Majumdar. Population-imbalanced lattice fermions near the BCS-BEC crossover: Thermal physics of the breached pair and Fulde-Ferrell-Larkin-Ovchinnikov phases. *Phys. Rev. A*, 93:053609, May 2016.

[23] J. Hubbard. Electron correlations in narrow energy bands. *Proceedings of the Royal Society of London A: Mathematical, Physical and Engineering Sciences*, 276(1365):238–257, 1963.

[24] H. Tasaki. The Hubbard model - an introduction and selected rigorous results. *Journal of Physics: Condensed Matter*, 10(20):4353, 1998.

[25] H. Fröhlich. Theory of the superconducting state. I. The ground state at the absolute zero of temperature. *Phys. Rev.*, 79:845–856, Sep 1950.

[26] T. Esslinger. Fermi-Hubbard physics with atoms in an optical lattice. *Annual Review of Condensed Matter Physics*, 1(1):129–152, 2010.

[27] P. Courteille, R. S. Freeland, D. J. Heinzen, F. A. van Abeelen, and B. J. Verhaar. Observation of a Feshbach resonance in cold atom scattering. *Phys. Rev. Lett.*, 81:69–72, Jul 1998.

[28] A. M. Clogston. Upper limit for the critical field in hard superconductors. *Phys. Rev. Lett.*, 9:266–267, Sep 1962.

[29] G. Sarma. On the influence of a uniform exchange field acting on the spins of the conduction electrons in a superconductor. *Journal of Physics and Chemistry of Solids*, 24(8):1029 – 1032, 1963.

[30] W. V. Liu and F. Wilczek. Interior gap superfluidity. *Phys. Rev. Lett.*, 90:047002, Jan 2003.

[31] S.-T. Wu and S. Yip. Superfluidity in the interior-gap states. *Phys. Rev. A*, 67:053603, May 2003.

[32] M. M. Forbes, E. Gubankova, W. V. Liu, and F. Wilczek. Stability criteria for breached-pair superfluidity. *Phys. Rev. Lett.*, 94:017001, Jan 2005.

[33] T. Koponen, J. Kinnunen, J.-P. Martikainen, L. M. Jensen, and P. Törmä. Fermion pairing with spin-density imbalance in an optical lattice. *New Journal of Physics*, 8(9):179, 2006.

[34] L. He and P. Zhuang. Stable sarma state in two-band fermi systems. *Phys. Rev. B*, 79:024511, Jan 2009.

[35] D.-H. Kim, J. S. J. Lehikoinen, and P. Törmä. Topological transitions of gapless paired states in mixed-geometry lattices. *Phys. Rev. Lett.*, 110:055301, Jan 2013.

[36] M. Tylutki and P. Törmä. Spin-Imbalanced Fermi Superfluidity in a Lieb Lattice Hubbard Model. *arXiv:1806.06964*, June 2018.

[37] H. Müther and A. Sedrakian. Spontaneous breaking of rotational symmetry in superconductors. *Phys. Rev. Lett.*, 88:252503, Jun 2002.

[38] A. Sedrakian, J. Mur-Petit, A. Polls, and H. Müther. Pairing in a two-component ultracold Fermi gas: Phases with broken-space symmetries. *Phys. Rev. A*, 72:013613, Jul 2005.

[39] T. K. Koponen, T. Paananen, J.-P. Martikainen, M. R. Bakhtiari, and P. Törmä. FFLO state in 1-, 2- and 3-dimensional optical lattices combined with a non-uniform background potential. *New Journal of Physics*, 10(4):045014, 2008.

[40] J. E. Baarsma and P. Törmä. Larkin-Ovchinnikov phases in two-dimensional square lattices. *Journal of Modern Optics*, 63(18):1795–1804, 2016.

[41] A. Georges, G. Kotliar, W. Krauth, and M. J. Rozenberg. Dynamical mean-field theory of strongly correlated fermion systems and the limit of infinite dimensions. *Rev. Mod. Phys.*, 68:13–125, Jan 1996.

[42] T. Maier, M. Jarrell, T. Pruschke, and M. H. Hettler. Quantum cluster theories. *Rev. Mod. Phys.*, 77:1027–1080, Oct 2005.

[43] G. Kotliar, S. Y. Savrasov, G. Pálsson, and G. Biroli. Cellular dynamical mean field approach to strongly correlated systems. *Phys. Rev. Lett.*, 87:186401, Oct 2001.

[44] M. H. Hettler, A. N. Tahvildar-Zadeh, M. Jarrell, T. Pruschke, and H. R. Krishnamurthy. Nonlocal dynamical correlations of strongly interacting electron systems. *Phys. Rev. B*, 58:R7475–R7479, Sep 1998.

[45] D.-H. Kim and P. Törmä. Fulde-ferrell-larkin-ovchinnikov state in the dimensional crossover between one- and three-dimensional lattices. *Phys. Rev. B*, 85:180508, May 2012.

[46] P. Kumar, T. I. Vanhala, and P. Törmä. Temperature and doping induced instabilities of the repulsive Hubbard model on the Lieb lattice. *Phys. Rev. B*, 96:245127, Dec 2017.

[47] M. Caffarel and W. Krauth. Exact diagonalization approach to correlated fermions in infinite dimensions: Mott transition and superconductivity. *Phys. Rev. Lett.*, 72:1545–1548, Mar 1994.

[48] A. Georges, G. Kotliar, W. Krauth, and Marcelo J. Rozenberg. Dynamical mean-field theory of strongly correlated fermion systems and the limit of infinite dimensions. *Rev. Mod. Phys.*, 68:13–125, Jan 1996.

[49] D. Sénéchal. An introduction to quantum cluster methods. *arXiv:0806.2690*, June 2008.

[50] T. I. Vanhala. *Dynamical mean-field theory studies of superfluidity and topological phases in lattice models.* PhD thesis, Aalto university, 2018.

[51] Y. Lu and M. W. Haverkort. Exact diagonalization as an impurity solver in dynamical mean field theory. *The European Physical Journal Special Topics*, 226(11):2549–2564, Jul 2017.

[52] F. F. Assaad and T. C. Lang. Diagrammatic determinantal quantum Monte Carlo methods: Projective schemes and applications to the Hubbard-Holstein model. *Phys. Rev. B*, 76:035116, Jul 2007.

[53] M. Kitatani, N. Tsuji, and H. Aoki. FLEX+DMFT approach to the d-wave superconducting phase diagram of the two-dimensional Hubbard model. *Phys. Rev. B*, 92:085104, Aug 2015.

[54] A. Toschi, A. A. Katanin, and K. Held. Dynamical vertex approximation: A step beyond dynamical mean-field theory. *Phys. Rev. B*, 75:045118, Jan 2007.

[55] A. N. Rubtsov, M. I. Katsnelson, and A. I. Lichtenstein. Dual fermion approach to nonlocal correlations in the Hubbard model. *Phys. Rev. B*, 77:033101, Jan 2008.

[56] G.-B. Jo, J. Guzman, C. K. Thomas, P. Hosur, A. Vishwanath, and D. M. Stamper-Kurn. Ultracold atoms in a tunable optical kagome lattice. *Phys. Rev. Lett.*, 108:045305, Jan 2012.

Appendix A

Mean-field theory

In this appendix, we give a short explanation of mean-field theory for the Hubbard model in the kagome lattice. This theory assumes fluctuations are small, so that the operator product $c^\dagger_{\uparrow,i}c^\dagger_{\downarrow,i}c_{\downarrow,i}c_{\downarrow,i}$ can be expressed as

$$c^\dagger_{\uparrow,i}c^\dagger_{\downarrow,i}c_{\uparrow,i}c_{\downarrow,i} \approx \left\langle c^\dagger_{\uparrow,i}c^\dagger_{\downarrow,i}\right\rangle c_{\downarrow,i}c_{\uparrow,i} + c^\dagger_{\uparrow,i}c^\dagger_{\downarrow,i}\left\langle c_{\downarrow,i}c_{\uparrow,i}\right\rangle - \left\langle c^\dagger_{\uparrow,i}c^\dagger_{\downarrow,i}\right\rangle\left\langle c_{\downarrow,i}c_{\uparrow,i}\right\rangle \tag{A.1}$$

$$+ \left\langle c^\dagger_{\uparrow,i}c_{\uparrow,i}\right\rangle c^\dagger_{\downarrow,i}c_{\downarrow,i} + c^\dagger_{\uparrow,i}c_{\uparrow,i}\left\langle c^\dagger_{\downarrow,i}c_{\downarrow,i}\right\rangle - \left\langle c^\dagger_{\uparrow,i}c^\dagger_{\uparrow,i}\right\rangle\left\langle c^\dagger_{\downarrow,i}c_{\downarrow,i}\right\rangle \tag{A.2}$$

$$- (\left\langle c^\dagger_{\uparrow,i}c_{\downarrow,i}\right\rangle c^\dagger_{\downarrow,i}c_{\uparrow,i} + c^\dagger_{\uparrow,i}c_{\downarrow,i}\left\langle c^\dagger_{\downarrow,i}c_{\uparrow,i}\right\rangle - \left\langle c^\dagger_{\uparrow,i}c^\dagger_{\downarrow,i}\right\rangle\left\langle c^\dagger_{\downarrow,i}c_{\uparrow,i}\right\rangle) \tag{A.3}$$

The pairing fields on the first line are related to the order parameter by $\tilde{\Delta}_i = U\left\langle c_{\downarrow,i}c_{\uparrow,i}\right\rangle$. The second line contains Hartree fields, which are commonly included as a shift in the chemical potential. The third line contains Fock fields, which are ignored in BCS mean field theory. With this approximation, the interaction term of the Hamiltonian becomes

$$H_{\text{int}} = U\sum_{i,\alpha} c^\dagger_{\uparrow i\alpha}c^\dagger_{\downarrow i\alpha}c_{\downarrow i\alpha}c_{\uparrow i\alpha} \tag{A.4}$$

$$\approx \sum_{i\alpha} c^\dagger_{\uparrow i\alpha}c^\dagger_{\downarrow i\alpha}\widetilde{\Delta_\alpha} + c_{\downarrow i\alpha}c_{\uparrow i\alpha}\widetilde{\Delta_\alpha}^* - |\widetilde{\Delta_\alpha}|^2/U. \tag{A.5}$$

Here, i labels the unit cells, and α the Bravais sublattices. In the FF ansatz, the order parameter is modulated by a plane wave: $\widetilde{\Delta_\alpha} = \Delta_\alpha e^{i\boldsymbol{q}\cdot\boldsymbol{x}}$. Taking the Fourier transform of the Hubbard Hamiltonian, we obtain

$$H = \sum_{\boldsymbol{k}} \left[\boldsymbol{c}_{\boldsymbol{k}}^{\dagger} \begin{pmatrix} H_{\boldsymbol{k}} - \mu_{\uparrow} & \boldsymbol{\Delta} \\ \boldsymbol{\Delta}^{\dagger} & -(H_{\boldsymbol{q}-\boldsymbol{k}}^{*} - \mu_{\downarrow}) \end{pmatrix} \boldsymbol{c}_{\boldsymbol{k}} + C \right], \tag{A.6}$$

$$C = -\sum_{\alpha=A}^{C} \left(\mu_{\downarrow} + \frac{|\Delta_{\alpha}|^2}{U} \right), \tag{A.7}$$

$$\boldsymbol{c}_{\boldsymbol{k}} = (c_{\boldsymbol{k}\uparrow A}, c_{\boldsymbol{k}\uparrow B}, c_{\boldsymbol{k}\uparrow C}, c_{\boldsymbol{q}-\boldsymbol{k}\downarrow A}^{\dagger}, c_{\boldsymbol{q}-\boldsymbol{k}\downarrow B}^{\dagger}, c_{\boldsymbol{q}-\boldsymbol{k}\downarrow C}^{\dagger})^T \tag{A.8}$$

The matrix $\boldsymbol{\Delta}$ is a diagonal matrix containing the order parameters. The kinetic energy matrix is the same as Eq. (2.8) in the main text.

As $H_{\boldsymbol{k}}$ is real and symmetric, it can be diagonalized: $H_{\boldsymbol{k}} = \mathcal{G}_{\boldsymbol{k}} \varepsilon_{\boldsymbol{k}} \mathcal{G}_{\boldsymbol{k}}^T$. The Hamiltonian is then rewritten

$$H = \sum_{\boldsymbol{k}} \left[\boldsymbol{d}_{\boldsymbol{k}}^{\dagger} \begin{pmatrix} \varepsilon_{\boldsymbol{k}} - \mu_{\uparrow} & \mathcal{G}_{\boldsymbol{k}}^T \boldsymbol{\Delta} \mathcal{G}_{\boldsymbol{q}-\boldsymbol{k}} \\ \mathcal{G}_{\boldsymbol{q}-\boldsymbol{k}}^T \boldsymbol{\Delta}^{\dagger} \mathcal{G}_{\boldsymbol{k}} & -(\varepsilon_{\boldsymbol{q}-\boldsymbol{k}}^{*} - \mu_{\downarrow}) \end{pmatrix} \boldsymbol{d}_{\boldsymbol{k}} + C \right], \tag{A.9}$$

$$\boldsymbol{d}_{\boldsymbol{k}} = (d_{\boldsymbol{k}\uparrow,1}, d_{\boldsymbol{k}\uparrow,2}, d_{\boldsymbol{k}\uparrow,3}, c_{\boldsymbol{q}-\boldsymbol{k}\downarrow,1}^{\dagger}, c_{\boldsymbol{q}-\boldsymbol{k}\downarrow,2}^{\dagger}, c_{\boldsymbol{q}-\boldsymbol{k}\downarrow,3}^{\dagger})^T. \tag{A.10}$$

This is the basis in which dispersion-band resolved densities and pairing correlations are computed.

The grand potential $\Omega = \mathrm{Tr}(\exp(-\beta H))$ is computed most easily in the basis that diagonalizes H. To determine the equilibrium state, the grand potential is minimized at fixed chemical potentials $\mu_{\uparrow}$ and $\mu_{\downarrow}$.